VORTEX NECKING PHENOMENA UNDER MICROGRAVITY

David Bean and Cable Kurwitz
Department of Nuclear Engineering, Texas A&M University

Dr. Fredrick Best and Purvi Waghela
Department of Nuclear Engineering, Texas A&M University

ABSTRACT

Vortex formation and stability is a function of the rotational velocity and the liquid inventory. Forces acting on the vortex, such as capillary and inertial forces, are dominant under different conditions. If the rotational velocity of the liquid is not sufficient, the desired cylindrical core required for separation does not occur. High velocities lead to instabilities and require excess power in terms of pressure head, which is undesirable. Texas A&M University has designed and fabricated a vortex type phase separator for use in microgravity. Furthermore, the Texas A&M University separator has been identified by Johnson Space Center for inclusion in the "Immobilized Microbe Microgravity Waste Water Processing System" (IMMWPS) shuttle experiment as part of a regenerative live support system. The focus of the investigation was to evaluate force balance predictions of operational boundary conditions of the phase separator. Results indicate that the ratio between forces acting on the vortex, inertial force and the capillary force, defined by the rotational Weber number, are optimized when the inertial force is approximately four times the magnitude of the capillary force.

INTRODUCTION AND BACKGROUND

Conservation and recycling of air and water is an important and necessary feature for long duration space missions. Since space systems are sensitive to volume, mass, and power, reutilization of the fluids is desired. Regenerative life support systems that recycle water are currently being investigated, which require phase separators to separate the liquid from the gas produced in biologic or chemical process systems. Typically, phase separation relies on capillary forces with a limited throughput or motor driven machines that require power and utilize moving parts that may reduce reliability. Vortex phase separators utilize the fluid's intrinsic momentum to produce a radial acceleration fields driving the separation process through buoyancy. Fluid momentum produces swirl, which forms a gas core surrounded by an annular liquid film during separator operation in microgravity. Vortex separators are completely passive having no moving parts, which is attractive in terms of power and reliability. Their compact and simple design are attractive in terms of mass and volume as well as control.

Microgravity two-phase flow is an important aspect of modern day space system applications. Therefore, development of separation technologies are required for advanced process systems. Currently, there are multiple types of separators: capillary separators that rely on capillary forces, through the use of wicks, to facilitate the separation process, hydrophilic/hydrophobic devices similar to capillary systems requiring special materials, mechanical separators are also very useful due to their high mass flows but require power, and vortex separators that have relatively high throughputs and are completely passive in operation. The focus of the experiment was to investigate a specific operational boundary condition for a unique vortex type phase separator developed at Texas A&M University. The purpose of the study was to determine the operational boundary conditions of the separator using the force balance approach and evaluate the predictions using data gathered onboard NASA's KC-135 aircraft. .

Phase separators are typically designed for specific applications ranging from thermal management systems, power generation and conservation, to advanced life support systems. Each separation system is designed for a particular application and typically the separator selected is specifically designed; thus, changes to the system will potentially require new separator type and/or design. For example, capillary style separators are good for low volumetric flow but are impractical for applications that require high flow rates. Vortex phase separators have proven to be relatively versatile in many different applications and may be integrated into different systems with little design change.

For space applications, vortex separators are extremely useful because they have no moving parts, which make them very reliable. Other than available pressure head, vortex separators require no power to operate, which is an important feature of any device that will operate in an environment where energy is limited. Vortex separators are also less prone to flooding or dry-out and can be designed to withstand all liquid or all gas injection for specific periods of time.

THEORY

Vortex phase separation is simple and straightforward. The Texas A&M phase separator is a right circular cylinder with inlet (nozzle) tangent to the inner cylinder wall, a gas outlet located along the axis of the cylinder opposite the liquid outlet located under the baffle plate as illustrated in Figure 1. Fluid is injected through the nozzle converting

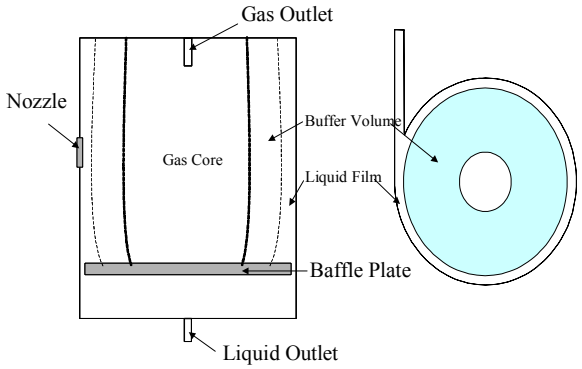

Figure 1: Texas A&M University Vortex Phase Separator

pressure head into velocity. The injected fluid momentum is coupled to the rotating system cylinder producing a rotational flow also known as swirl. Due to the radial acceleration produced by the swirl, the dense liquid remains near the wall and the less dense gas migrates radially inward forming a vortex along the center axis of the cylinder. As the body forces are reduced, the vortex depression becomes deeper. Neglecting capillary forces, under zero gravity conditions, the vortex takes the shape of a cylinder made up of the low-density gas surrounded by an annulus of dense liquid.[3]

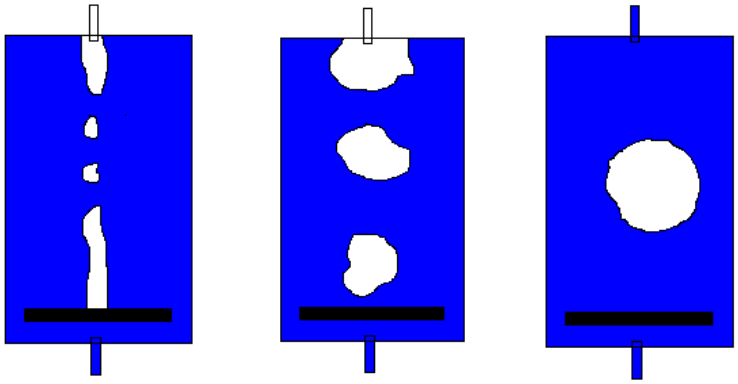

Figure 2: Various Representations of Necking Phenomena

The focus of the investigation was to evaluate the prediction of the phenomena know as "necking." Necking, shown in Figure 2, is observed at small gas core diameters and/or low rotational speeds as capillary forces attempt to draw the bubble into a shape of low surface energy. As the magnitude of the capillary forces increase, the shape of the vortex changes to reduce the surface energy becoming spherical. For small diameter cylinders, the liquid may bridge the core of the gas cylinder into two or more parts; hence, the name "necking." As seen in Figure 2, the small diameter vortex has broken into a number of

parts due to capillary bridging of the gas core. This will occur sufficiently low rotational speeds and at small gas core diameters. Since there are minor axial velocity gradients due to the end caps, the gas core may take the form of a sphere, which is due to the same phenomenon but occurs at larger gas core diameters.

To predict the occurrence of the necking phenomenon, a force balance approach is utilized. This development is similar to that found in Theoretical Hydrodynamics by Milne-Thomson[1]. Using groups of dimensionless parameter, one may deduce a relationship that describes the ratio of inertial to surface tension forces acting on the liquid. Starting with the Bond number (Bo), the ratio of acceleration force to surface tension force, shown in Equation 1 and the Froude number (Fr), the ratio of inertial force to acceleration force shown in Equation. 2, the rotational Weber number (Equation 4),

$$Bo = \frac{acceleration\ \ force}{surface\ \ tension\ \ force} = \frac{\left(\rho_l - \rho_g\right) R_I^2 g}{\sigma} \qquad \textbf{Eq. 1}$$

$$Fr = \frac{inertial\ \ force}{acceleration\ \ force} = \frac{V^2}{gD_I} \qquad \textbf{Eq. 2}$$

can be produced by multiplying the Bond and Froude numbers resulting in the ratio of inertial force to capillary force. To account for rotation, Equation 2 is modified to account for circular motion as see in Equation 3. Rearranging, the relationship to the

$$V = \omega R_I \qquad \textbf{Eq. 3}$$

rotational Weber number is shown in Equation 4, which relates the gas core diameter to the rotational speed. Equation 5 is the rotational Weber number as a function of the gas core diameter and the rotational speed of the fluid is plotted in Figure 3. .

$$\begin{aligned} We = Bo \cdot Fr = \frac{inertial\ \ force}{surface\ tension\ \ force} = \\ \frac{\left(\rho_l - \rho_g\right) R_I^2 g}{\sigma} \frac{V^2}{gD_I} = \frac{\left(\rho_l - \rho_g\right) D_I^2 g}{4\sigma} \frac{R_I^2 \omega^2}{gD_I} \\ = \frac{\left(\rho_l - \rho_g\right) R_I^2 D_I \omega^2}{4\sigma} = \frac{\left(\rho_l - \rho_g\right) R_I^3 \omega^2}{2\sigma} \end{aligned} \qquad \textbf{Eq. 4}$$

Another attractive feature of the Texas A&M vortex phase separator is the buffer volume

$$D_I = 2\sqrt[3]{\frac{2\sigma We}{\left(\rho_l - \rho_g\right)\omega^2}} \qquad \textbf{Eq. 5}$$

shown in Figure 1. Depending on the design, the buffer volume allows the separator to operate for specified periods of all liquid or all gas injection. Therefore, a mismatch in the inlet and outlet volumetric flow of liquid can be handled with a corresponding decrease or increase in the thickness of the liquid of the annulus. Limitations associated

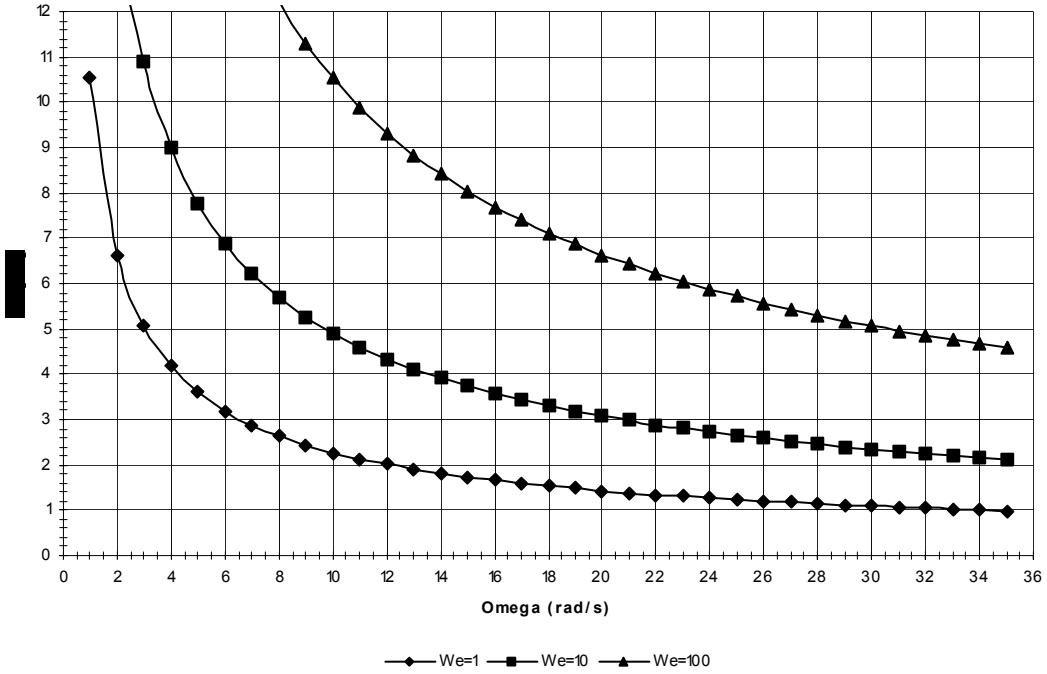

Figure 3: Rotational Weber Number as a Function of Gas Core Diameter and Rotational Speed.

with buffer volume size relate to hydrodynamic phenomena characterized as "carry-over" (flooding- liquid in air outlet) and "carry under" (dry out- air in liquid outlet) illustrated in Figures 4 and 5. This phenomenon is detailed in work by Kurwitz et al and Ellis et al.[4]

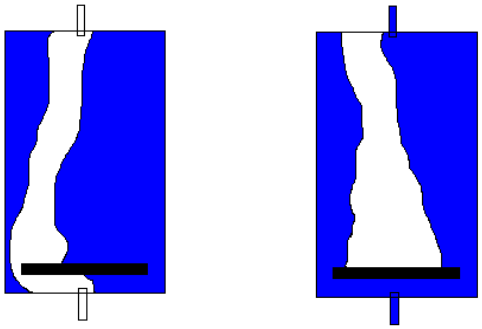

Figure 4: Carry Under **Figure 5: Carry Over**

EXPERIMENTAL SETUP

A clear, instrumented separator was the flight article integrated into a recirulating test loop shown in Figure 6. Liquid was circulated to and from the separator using a gear pump. Two differential pressure transducers measuring the radial pressure drop within the separator and the pressure drop across the nozzle were installed as shown in Figure 6. Liquid inventory adjustment was accomplished using two three-way valves and a separate storage tank. Volumetric flow, pump speed, radial differential pressure, nozzle differential pressure, and acceleration (Triaxial accelerometer not shown) data was recorded using a laptop PC running Labview. The clear, plastic separator allowed

operators to view the vortex and note the occurrence of "necking." Video footage of the vortex was also recorded.

NASA's KC-135 aircraft flies a series of parabolic trajectories shown in Figure 7 to achieve the desired acceleration level. The KC-135 aircraft can produce approximately 20 seconds of near zero gravity, ≈ ±0.01g. Typically, four sets of ten consecutive parabolas are flown followed by a short period of level flight between each set. Therefore, the test matrix each flight day consists of four different liquid volumes corresponding to specific gas core diameters tested over a range of flow rates to vary the rotational speed.

Vortex diameters were varied by raising or lowering the liquid level in 1g during level flight. Assuming the gas core is modeled by

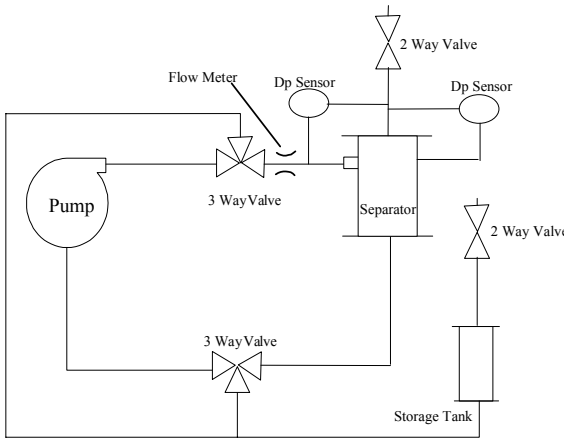

Fig 6: Test Loop Schematic

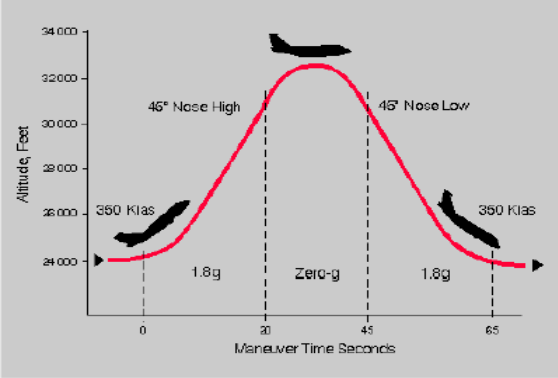

Fig 7: KC-135 Flight Trajectory (taken from http://jsc-aircraft-ops.jsc.nasa.gov/kc135/index.html)

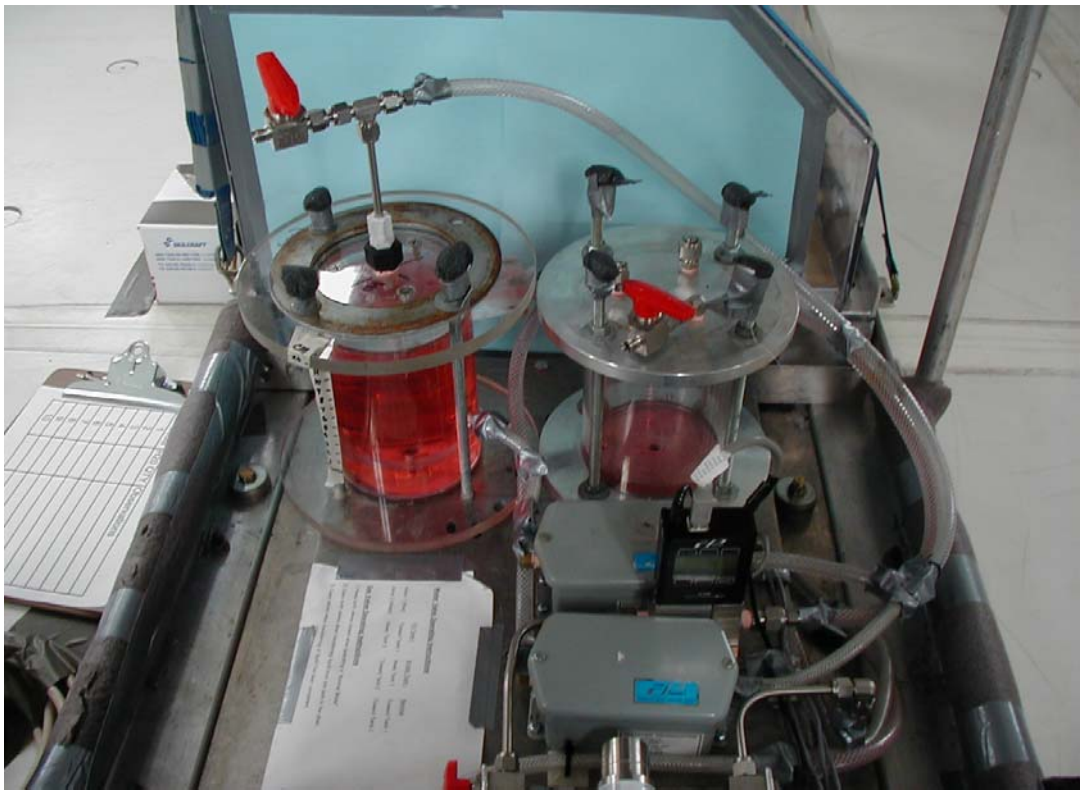

Fig 6a: Test Loop

a cylinder, the desired core diameter can be related to liquid fill height using Equation 6.

$$\frac{D_l}{D} = \left[1 - \frac{h}{H}\right]^{1/2} \qquad \textbf{Eq. 6}$$

The rotational speed was varied each parabola by changing pump speed (flow rate). Visual data was recorded using a video camera and a logbook to document observations about the quality of the vortex.

DATA ANALYSIS AND RESULTS

Six flights were carried out with approximately 240 test points recorded. Data over a range of flow rates (397-4028.2 mL/min.) was tested at various fill levels (6-11 cm). Observations were made for each parabola including environmental conditions such as negative acceleration. Data reduction consisted of a number of filters to formalize results based on hydrodynamic phenomena only. Thus, perturbations produced by equipment problems or adverse environmental conditions were eliminated from the data set

The first filter was elimination of data associated with equipment malfunction. This includes malfunctions not directly affecting the separator loop but diverting attention of the operator to record his observations. The second filter involved the analysis of the triaxial acceleration for each parabola. Not only does the required average acceleration be less than ≈ ±0.01g but also the magnitude of the vertical acceleration could not rise above ±0.025g. Further, each parabola was limited temporally to the time spent within the previously stated limits. Parabolas that did not meet filtering process were eliminated from the data set. The resulting data points are listed in the Table 1 in the Appendix with corresponding visual observation in regard to the "necking" phenomena.

Equation 7 was derived to determine the radial hydrostatic head produced from the circular rotation of the liquid. Solving for the rotational speed, ω, and the gas core diameter (D_l) from the fill height, h, one can plot the data as compared to the rotational Weber number shown in Figure 8. With D_l and ω known, we can calculate the rotational Weber number using Equation 5 and determine the ratio of forces that produce a stable interface.

$$\Delta P = \frac{\left(\rho_l - \rho_g\right)\omega^2}{8}\left(D^2 - D_l^2\right) \qquad \textbf{Eq.7}$$

As expected, desired cylindrical vortex arrangements are found at high rotational speeds and larger gas core diameters where inertial forces dominate. Figure 8 also provides the predicted error based on the accuracy of the differential pressure transducer and fill level measurement. Results indicate the inertial force must be approximately 2 orders of magnitude greater than the capillary force for necking not to occur and also indicate that the force balance approach is a useful tool to evaluate vortex conditions. This provides a bounding limit to the design and operation of vortex style phase separators.

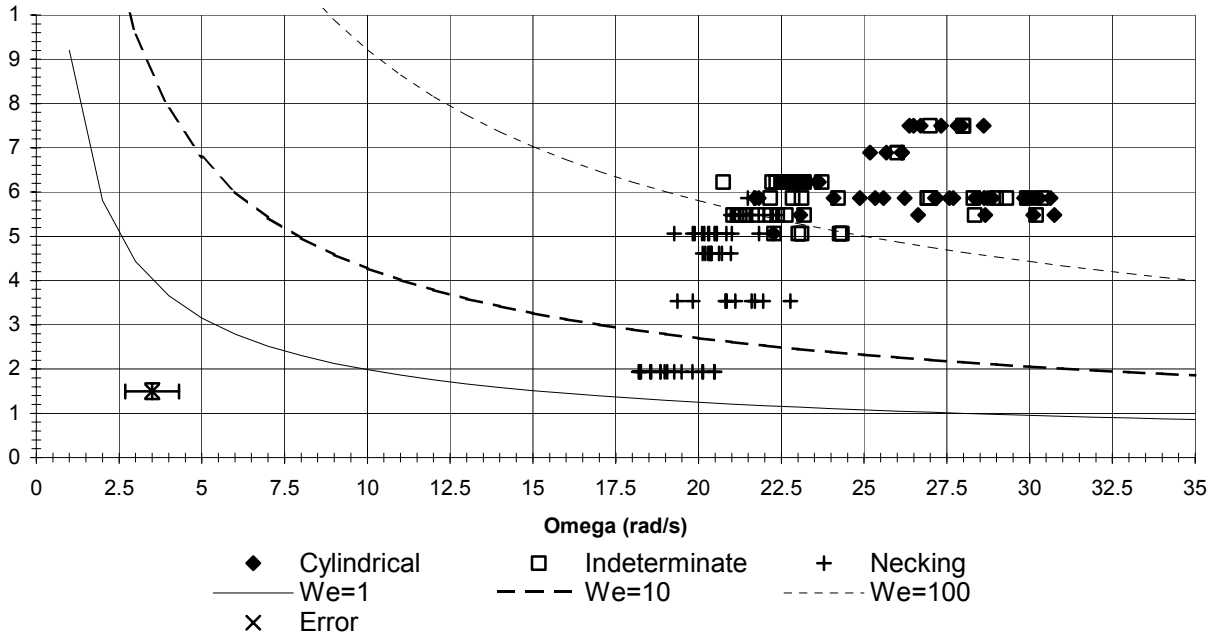

Figure 8: Test Results Compared to Rotational Weber Number

CONCLUSIONS

The necking phenomenon was modeled using a force balance approach. Successful vortex formation occurs when the inertial forces dominate the capillary forces by 2 orders of magnitude. Understanding this boundary condition will allow designers to optimize the size of the separator leading to reduced power consumption, and increased confidence in successful operation.

A secondary objective has been to collect data to assess the possibility of using the radial differential pressure transducer as a method of determining the liquid annulus thickness, buffer volume. Assuming a constant rotational speed corresponding to a constant pump speed (i.e. inlet flow rate) one can relate radial differential pressure to gas core diameter and liquid thickness using Equation 7. Analysis is still being carried out with promising initial results.

ACKNOWLEDGEMENTS

The authors would like to thank the members of the Interphase Transport Phenomena Laboratory and the Center for Space Power at Texas A&M University for use of the hardware and integration into the flight package. Furthermore the authors greatly appreciate NASA JSC Crew and Thermal Systems and specifically Dr. Katy Hurlbert for supporting this investigation.

REFERENCES

1. Milne-Thomson, L. M. *Theoretical Hydrodynamics*. New York: The Macmillan Company.

2. Knoll, Glenn F. *Radiation Detection and Measurement, 2nd Ed.* New York: John Wiley & Sons, 1989

3. M. Ellis and F. Best, "Experimental and Analytical Results of a Liquid-Gas Separator in Microgravity," Proceedings of the Conference on Applications of Thermophysics in Microgravity and Breakthrough Propulsion Physics, Albuquerque, New Mexico, January 1999.

4. C. Kurwitz and F. Best, "Phase Separation By Passively Induced Centrifugal Forces," 4th International Conference on Life Support and Biosphere Science, Baltimore, MD. August,2000.

Nomenclature

Bo.....Bond Number
D_I.....Gas Core Diameter
D.....Diameter of separator
F .....Froude Number
H.....Height of cylinder
R_I .....Gas Core Radius
V.....Velocity
We .....Weber Number
g.....Gravitational Acceleration
h.....Fluid Fill Level
ρ_l.....Density of water
ρ_g .....Density of air
σ .....Surface tension of water at 25°C
ω.....Azimuthal Velocity

APPENDIX

ERROR

For any study to have meaning, there must me some measure of confidence of the accuracy of our calculations. The following is how the error associated with our measurements was determined.

To find the error of the radial velocity and normalized gas core diameter (D_i/D) we used equations from Radiation Detection and Measurement[2]. For the radial velocity, we first took the sum all the points as described in this equation:

$$\Sigma = \omega_1 + \omega_2 + ...\omega_N$$

Next, to find the error in calculation of the radial velocity, we applied the error propagation formula. Since we had multiple points, we needed a measurement of a single count. Thus the result shows the standard deviation as a single count.

$$\sigma_\Sigma^2 = \sigma_{\omega_1}^2 + \sigma_{\omega_2}^2 + ...\sigma_{\omega_N}^2$$

We also need to calculate the mean value from the independent measurements *N*. Thus to find the mean value, we used the following equation,

$$\bar{\omega} = \frac{\Sigma}{N}$$

Finally, we calculated the expected error by relating the mean value to the independent measurements using following equation.

$$\sigma_{\bar{\omega}} = \sqrt{\frac{\bar{\omega}}{N}}$$

Radial velocity varied with each data point, however the normalized gas core diameter varied only with every set of ten parabolas. Therefore, we had to use a different set of equations to find the error associated with the gas core diameter. We did not have to find the sum since we only had one point for every set of ten parabolas. To calculate the error for a point we applied the following equation:

$$\left(\frac{\sigma_{D_i}}{D_i}\right)^2 = \left(\frac{\sigma_{\bar{\omega}}}{\bar{\omega}}\right)^2$$

We eliminated σ_D/D because we did not have an error finding D. Thus we solved for σ_{Di} to get our error and divided it by the diameter of the separator. After calculating the error for the radial velocity and gas core diameter, we determined that we had an error <1% for the radial velocity, and an error <0.5% for the gas core diameter.

FILL LEVEL TO GAS CORE DIAMETER RELATION

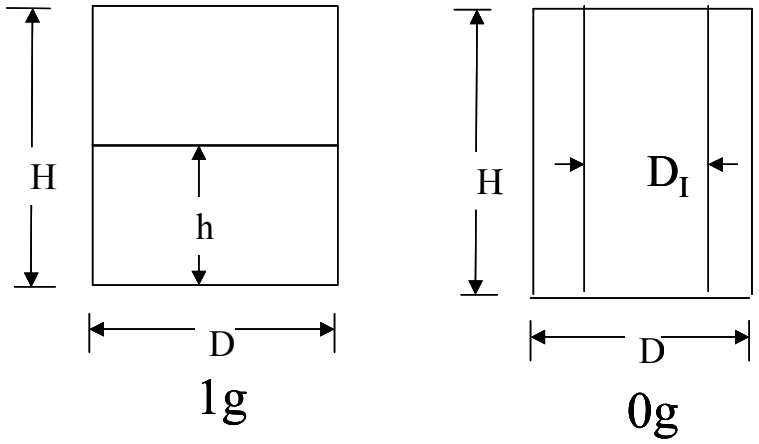

$$vol_{1_g} = vol_{0_g}$$

$$\frac{\Pi D^2 h}{4} = \frac{\Pi D^2 H}{4} - \frac{\Pi D_I^2 H}{4}$$

$$D^2 h = D^2 H - D_I^2 H \quad \rightarrow \quad \frac{D_I^2}{D^2} H = H - h$$

$$\frac{D_I^2}{D^2} = 1 - \frac{h}{H} \quad \rightarrow \quad \frac{D_I}{D} = \sqrt{1 - \frac{h}{H}}$$

Table 1 Vortex Stability Observation

Parabola Number	Omega (rad/s)	D_I/D	Vortex Stability
ALS Day 2 #1	20.48003642	0.194	B
ALS Day 2 #2	20.47208846	0.194	B
ALS Day 2 #3	20.13438113	0.194	B
ALS Day 2 #4	18.9726597	0.194	B
ALS Day 2 #5	19.4840662	0.194	B
ALS Day 2 #6	19.04884722	0.194	B
ALS Day 2 #7	19.26866452	0.194	B
ALS Day 2 #8	18.84709078	0.194	B
ALS Day 2 #9	20.11883958	0.194	B
ALS Day 2 #10	19.81653762	0.194	B
ALS Day 2 #11	21.94944075	0.3537	B
ALS Day 2 #12	22.77023317	0.3537	B
ALS Day 2 #13	20.81506605	0.3537	B
ALS Day 2 #15	21.11186046	0.3537	B
ALS Day 2 #16	19.82718895	0.3537	B
ALS Day 2 #17	20.84892622	0.3537	B
ALS Day 2 #18	19.36383552	0.3537	B
ALS Day 2 #19	21.60363564	0.3537	B
ALS Day 2 #20	21.6986776	0.3537	B
ALS Day 2 #21	24.325104	0.5063	I
ALS Day 2 #22	24.26013479	0.5063	I
ALS Day 2 #23	23.1114619	0.5063	I
ALS Day 2 #24	23.01449537	0.5063	I
ALS Day 2 #25	22.28296003	0.5063	I
ALS Day 2 #26	22.26062357	0.5063	G
ALS Day 2 #27	20.55440068	0.5063	B
ALS Day 2 #28	20.31348237	0.5063	B
ALS Day 2 #29	19.88154398	0.5063	B
ALS Day 2 #30	19.26555552	0.5063	B
ALS Day 2 #31	26.2208179	0.5864	G
ALS Day 2 #33	25.33549911	0.5864	G
ALS Day 2 #34	24.87099891	0.5864	G
ALS Day 2 #35	24.07922448	0.5864	G
ALS Day 2 #36	24.21071057	0.5864	I
ALS Day 2 #37	23.11557823	0.5864	I
VCD Day 1 #1	23.0679905	0.5478	G
VCD Day 1 #2	23.1931525	0.5478	I
VCD Day 1 #3	22.6325882	0.5478	I
VCD Day 1 #4	22.3784717	0.5478	I
VCD Day 1 #5	22.3489119	0.5478	B
VCD Day 1 #6	22.1785013	0.5478	I
VCD Day 1 #7	22.2457242	0.5478	B
VCD Day 1 #8	21.2694949	0.5478	B
VCD Day 1 #9	21.7688106	0.5478	I
VCD Day 1 #10	21.8134831	0.5478	B

VCD Day 1 #11	22.7539688	0.6226	G
VCD Day 1 #12	22.8342487	0.6226	G
VCD Day 1 #13	22.536995	0.6226	G
VCD Day 1 #14	22.7064643	0.6226	G
VCD Day 1 #15	22.5618052	0.6226	I
VCD Day 1 #16	22.5573416	0.6226	B
VCD Day 1 #18	22.552121	0.6226	I
VCD Day 1 #19	22.2216677	0.6226	I
VCD Day 1 #20	20.7424796	0.6226	I
VCD Day 1 #22	26.1504272	0.6893	G
VCD Day 1 #23	26.1412574	0.6893	G
VCD Day 1 #25	25.9975168	0.6893	I
VCD Day 1 #26	25.6724214	0.6893	B
VCD Day 1 #30	25.1820782	0.6893	B
VCD Day 1 #31	28.6121449	0.7500	G
VCD Day 1 #32	27.3218273	0.7500	G
VCD Day 1 #33	26.9906089	0.7500	I
VCD Day 1 #34	26.7030741	0.7500	G
VCD Day 1 #35	27.9915501	0.7500	I
VCD Day 1 #36	27.9980664	0.7500	I
VCD Day 1 #37	26.3650987	0.7500	G
VCD Day 1 #38	27.8205974	0.7500	B
VCD Day 1 #39	26.4940075	0.7500	B
VCD Day 1 #40	27.9455678	0.7500	B
VCD Day 2 #2	18.84919211	0.1940	B
VCD Day 2 #3	18.56847274	0.1940	B
VCD Day 2 #4	18.53536759	0.1940	B
VCD Day 2 #5	18.22512358	0.1940	B
VCD Day 2 #7	18.22363783	0.1940	B
VCD Day 2 #8	18.19284696	0.1940	B
VCD Day 2 #10	18.26276859	0.1940	B
VCD Day 2 #11	20.97857066	0.4611	B
VCD Day 2 #12	20.61977585	0.4611	B
VCD Day 2 #13	20.70056586	0.4611	B
VCD Day 2 #14	20.39935572	0.4611	B
VCD Day 2 #15	20.12805314	0.4611	B
VCD Day 2 #16	20.32424648	0.4611	B
VCD Day 2 #17	20.37810435	0.4611	B
VCD Day 2 #18	20.20087418	0.4611	B
VCD Day 2 #19	20.29180668	0.4611	B
VCD Day 2 #21	23.57671076	0.6226	G
VCD Day 2 #22	23.7192768	0.6226	I
VCD Day 2 #23	23.05388338	0.6226	I
VCD Day 2 #24	23.1499174	0.6226	B
VCD Day 2 #25	22.86299093	0.6226	B
VCD Day 2 #26	23.18736815	0.6226	I
VCD Day 2 #30	22.81405667	0.6226	I
VCD Day 3 #2	21.82920081	0.5063	B
VCD Day 3 #3	21.00306688	0.5063	B
VCD Day 3 #4	20.84060018	0.5063	B
VCD Day 3 #5	20.54785859	0.5063	B
VCD Day 3 #6	20.47853186	0.5063	B
VCD Day 3 #7	20.17663264	0.5063	B
VCD Day 3 #8	19.82417022	0.5063	B
VCD Day 3 #9	20.28914601	0.5063	B

VCD Day 3 #10	20.10953296	0.5063	B
VCD Day 3 #11	21.24134595	0.5478	I
VCD Day 3 #12	21.35052561	0.5478	B
VCD Day 3 #14	21.42124409	0.5478	I
VCD Day 3 #15	21.5411743	0.5478	B
VCD Day 3 #16	21.09997221	0.5478	B
VCD Day 3 #17	21.04463077	0.5478	I
VCD Day 3 #18	20.97653136	0.5478	B
VCD Day 3 #19	21.02264848	0.5478	B
VCD Day 3 #21	22.8394951	0.5864	I
VCD Day 3 #22	22.16030441	0.5864	I
VCD Day 3 #25	21.81273129	0.5864	G
VCD Day 3 #26	21.70510742	0.5864	G
VCD Day 3 #27	21.48615117	0.5864	B
VCD Day 3 #29	21.6736263	0.5864	B
VCD Day 3 #31	23.6363302	0.6226	G
VCD Day 3 #33	23.11687981	0.6226	G
VCD Day 3 #35	22.35170798	0.6226	I
VCD Day 3 #36	22.63375959	0.6226	I
VCD Day 3 #37	22.49201579	0.6226	I
VCD Day 3 #38	23.28338354	0.6226	G
VCD Day 3 #39	23.22862086	0.6226	G
VCD Day 3 #40	23.08554024	0.6226	B

SAMPLE ACCELERATION GRAPH